


# Pattern description of quantum phase transitions in the transverse antiferromagnetic Ising model with a longitudinal field

Yun-Tong Yang(杨赟彤), Fu-Zhou Chen(陈富州), and Hong-Gang Luo(罗洪刚)
**Citation:**Chin. Phys. B, 2025, 34 (**12**): 127504. DOI: 10.1088/1674-1056/ae1564
http://cpb.iphy.ac.cn; http://iopscience.iop.org/cpb

**What follows is a list of articles you may be interested in**

---

## Accurate quantum critical points and nonlocal string order parameters in the spin tetrahedron chain

Zhi-Yong Wu(吴志勇), Kai-Ming Zhang(张凯铭), and Li-Xiang Cen(岑理相)
Chin. Phys. B, 2025, 34 (**11**): 117502. DOI: 10.1088/1674-1056/ae0c7c

## Scaling corrections in driven critical dynamics: Application to the two-dimensional dimerized quantum Heisenberg model

Jing-Wen Liu(刘静雯), Shuai Yin(阴帅), and Yu-Rong Shu(舒玉蓉)
Chin. Phys. B, 2025, 34 (**5**): 057502. DOI: 10.1088/1674-1056/adc672

## Off-diagonal approach to the exact solution of quantum integrable systems

Yi Qiao(乔艺), Junpeng Cao(曹俊鹏), Wen-Li Yang(杨文力), Kangjie Shi(石康杰), and Yupeng Wang(王玉鹏)
Chin. Phys. B, 2023, 32 (**11**): 117504. DOI: 10.1088/1674-1056/ad0774

## Emergent O(4) symmetry at the phase transition from plaquette-singlet to antiferromagnetic order in quasi-two-dimensional quantum magnets

Guangyu Sun(孙光宇), Nvsen Ma(马女森), Bowen Zhao(赵博文), Anders W. Sandvik, and Zi Yang Meng(孟子杨)
Chin. Phys. B, 2021, 30 (**6**): 067505. DOI: 10.1088/1674-1056/abf3b8

## Tunable deconfined quantum criticality and interplay of different valence-bond solid phases

Bowen Zhao(赵博文), Jun Takahashi, Anders W. Sandvik
Chin. Phys. B, 2020, 29 (**5**): 057506. DOI: 10.1088/1674-1056/ab889b

---

**RAPID COMMUNICATION**

# Pattern description of quantum phase transitions in the transverse antiferromagnetic Ising model with a longitudinal field

Yun-Tong Yang(杨赟彤)[1,2], Fu-Zhou Chen(陈富州)[1,2], and Hong-Gang Luo(罗洪刚)[1,2,†]

[1] *School of Physical Science and Technology, Lanzhou University, Lanzhou* 730000, *China*
[2] *Lanzhou Center for Theoretical Physics, Key Laboratory of Theoretical Physics of Gansu Province, Key Laboratory of Quantum Theory and Applications of MoE, Gansu Provincial Research Center for Basic Disciplines of Quantum Physics, Lanzhou University, Lanzhou* 730000, *China*

(Received 4 July 2025; revised manuscript received 4 September 2025; accepted manuscript online 21 October 2025)

A uniform longitudinal field applied to the transverse Ising model (TIM) distinguishes the antiferromagnetic Ising interaction from its ferromagnetic counterpart. While the ground state of the latter shows no quantum phase transition (QPT), the ground state of the former exhibits rich phases: paramagnetic, antiferromagnetic, and possibly disordered phases. Although the first two are clearly identified, the existence of the disordered phase remains controversial. Here, we use the pattern picture to explore the competition among the antiferromagnetic Ising interaction $J$, the transverse field $h_x$ and the longitudinal field $h_z$, and uncover which patterns are responsible for these three competing energy scales, thereby determining the possible phases and the QPTs among them. The system size ranges from $L = 8$ to 128 and the transverse field $h_x$ is fixed at 1. Under these parameters, our results show the existence of the disordered phase. For a small $h_z$, the system transitions from a disordered phase to an antiferromagnetic phase as $J$ increases. For a large $h_z$, the system undergoes two phase transitions: from paramagnetic to disordered, and then to antiferromagnetic phase. These results not only unveil the rich physics of this paradigmatic model but also stimulate quantum simulation by using currently available experimental platforms.

**Keywords:** pattern picture, quantum phase transitions, antiferromagnetic Ising model

**PACS:** 75.10.Pq, 75.40.Mg, 68.35.Rh

**DOI:** 10.1088/1674-1056/ae1564 **CSTR:** 32038.14.CPB.ae1564

## 1. Introduction

The Lenz–Ising model introduced initially in order to explain ferromagnetism[1–3] plays a paradigmatic role in many branches of modern physics, such as statistical physics[4,5] and condensed matter physics.[6–9] In particular, it is one of the central models in quantum simulation[10–17] and quantum annealing.[18–21] The intriguing physics of such a model originates from the fact that it can exhibit a thermodynamic phase transition from a paramagnetic phase at high temperature to a ferromagnetic phase at low temperature in the two-dimensional (2D) case, which was obtained by Onsager in 1944 in a mathematically exact form.[22] This triggered the development of modern statistical physics, in which the key concepts of universality class and critical scaling related to phase transitions have been introduced and described by critical exponents in renormalization group theory.[23] Thus the study of finding and classifying new phase transitions remains one of the scientific frontiers in current condensed matter physics, statistical physics, and related disciplines.

In the one-dimensional (1D) case, as demonstrated by Ising,[2] thermal fluctuations completely destroy the system's ordering, leading to the absence of thermodynamic phase transitions; however, at absolute zero temperature, with the disappearance of thermal excitations, the system may achieve an ordered ground state, where introducing quantum fluctuations can potentially induce a quantum phase transition (QPT).[7–9] The 1D transverse-field Ising model serves as the simplest paradigmatic system in this context,[24] where adjusting the ratio between the Ising interaction strength and the transverse magnetic field clearly exhibits a QPT from a disordered phase to an ordered ferromagnetic phase. It was found that such a QPT follows the standard universality class of the classical 2D Ising model. Furthermore, the situation becomes more intriguing once an extension term such as a longitudinal magnetic field, long-range interaction, or frustration is introduced.

In this work, we focus on the simplest scenario of introducing a longitudinal magnetic field. In the case of a ferromagnetic Ising interaction, the QPT in the ground state is smeared out. Conversely, for the antiferromagnetic case, the situation becomes more complex and exhibits richer physics, as three competing energy scales govern the system's behavior: the antiferromagnetic Ising interaction flavors an alternating alignment of up and down spins, and the longitudinal field prefers to align all spins along the direction of the field while the transverse field introduces quantum fluctuations, driving possible QPTs in the system. Intuitively, two phases must ex-

[†]Corresponding author. E-mail: luohg@lzu.edu.cn

© 2025 Chinese Physical Society and IOP Publishing Ltd. All rights, including for text and data mining, AI training, and similar technologies, are reserved.

ist: the antiferromagnetic one if the antiferromagnetic Ising interaction dominates over the others and the paramagnetic one if the longitudinal field is strong enough. How about the third case, namely, the transverse field is predominant over the others? This constitutes the first controversy of the model. State-of-the-art numerical techniques including exact diagonalization (ED),[25] density matrix renormalization group (DMRG)[26–28] and quantum Monte Carlo (QMC)[29] consistently identify only antiferromagnetic and paramagnetic phases, a finding corroborated by ultracold atom quantum simulations.[11] However, the fidelity susceptibility analyses challenge this conclusion by suggesting an additional disordered phase.[30] Furthermore, the nature of the phase transition itself in this model remains debated, with some studies proposing a continuous phase transition from antiferromagnetic phase to paramagnetic phase,[25,30] while others argue for a more complex mixed-order or hybrid-type transition that defies conventional classification.[17,28,31–36]

Here we investigate the antiferromagnetic transverse-field Ising model in the presence of a longitudinal field by employing the pattern picture method,[37] which is a novel approach we developed for extracting information from Hamiltonians. The method involves reconstructing the Hamiltonian in the space formed by spin operators $\{\hat{\sigma}_1^x, \mathrm{i}\hat{\sigma}_1^y, \hat{\sigma}_1^z, \hat{\sigma}_2^x, \mathrm{i}\hat{\sigma}_2^y, \hat{\sigma}_2^z, \ldots, \hat{\sigma}_L^x, \mathrm{i}\hat{\sigma}_L^y, \hat{\sigma}_L^z\}$, decomposing the original Hamiltonian into multiple components (expressed as $\hat{H} = \sum_n \hat{H}_n$), and then using ED and DMRG methods to obtain the system's ground state wavefunctions and projecting them onto different Hamiltonian components $\hat{H}_n$ to determine phases through their intersection points. For a fixed transverse field $h_x$, we calculate the ground state energy and its components as functions of the antiferromagnetic Ising interaction $J$ and the longitudinal field $h_z$ for lattice sizes up to 128 spins. The results show that the system transitions directly from the disordered phase to the antiferromagnetic phase as $J$ increases for small $h_z$, whereas at large $h_z$, the system first transitions from the paramagnetic phase to the disordered phase before transitioning to the antiferromagnetic phase.

The paper is organized as follows. In Section 2, we introduce the model and the pattern picture. In Section 3, we first calculate the ground state energy and its components for a lattice size of $L = 8$ and analyze the responses of different patterns to the Ising interaction and the longitudinal field; then we extend our analysis to large lattice sizes ranging from $L = 16$ to 128. Finally, Section 4 is devoted to a brief conclusion and discussion.

## 2. Model and method

The Hamiltonian of the transverse antiferromagnetic Ising model with a longitudinal field reads

$$\hat{H}' = J' \sum_{j,\delta} \hat{\sigma}_j^z \hat{\sigma}_{j+\delta}^z - h_z' \sum_j \hat{\sigma}_j^z - h_x \sum_j \hat{\sigma}_j^x, \tag{1}$$

where $J'$ is assumed to be non-negative, which denotes the antiferromagnetic Ising interaction between two spins represented by Pauli matrices $\hat{\sigma}^z$ located at site $j$ and its nearest neighbors $j+\delta$. $h_z'$ and $h_x$ denote the longitudinal and transverse fields, respectively.

### 2.1. A novel formulation of the Hamiltonian

In what follows, we take the transverse field $h_x$ as the units of energy, and take $h_x = 1$, so quantum fluctuations always exist in the present context. Equation (1) is rewritten as

$$\hat{H}' = \frac{h_x}{2}\hat{H}, \quad \hat{H} = \sum_j \hat{H}_j, \tag{2}$$

$$\hat{H}_j = -2\hat{\sigma}_j^x - 2h_z\hat{\sigma}_j^z + J\sum_\delta \left(\hat{\sigma}_j^z\hat{\sigma}_{j+\delta}^z + \hat{\sigma}_{j+\delta}^z\hat{\sigma}_j^z\right), \tag{3}$$

where $J = J'/h_x$ and $h_z = h_z'/h_x$. Using the identities $\hat{\sigma}^x\hat{\sigma}^y = \mathrm{i}\hat{\sigma}^z$ and $\hat{\sigma}^y\hat{\sigma}^z = \mathrm{i}\hat{\sigma}^x$, the Hamiltonian (3) can be rewritten as

$$\begin{aligned}\hat{H}_j \;=\; & 2\left(\mathrm{i}\hat{\sigma}_j^y\right)\hat{\sigma}_j^z + 2h\hat{\sigma}_j^x\left(\mathrm{i}\sigma_j^y\right) \\ & + J\sum_\delta \left(\hat{\sigma}_j^z\hat{\sigma}_{j+\delta}^z + \hat{\sigma}_{j+\delta}^z\hat{\sigma}_j^z\right).\end{aligned} \tag{4}$$

For a chain with size $L$ under periodic boundary condition (PBC) (i.e., $\hat{\sigma}_{L+1}^z = \hat{\sigma}_1^z$), $\hat{H}$ can be reformulated as a $3L \times 3L$ matrix in a spin operator space as follows:

$$\begin{aligned}\hat{H} \;=\; & \left(\begin{array}{cccccccccc}\hat{\sigma}_1^x & -\mathrm{i}\hat{\sigma}_1^y & \hat{\sigma}_1^z & \hat{\sigma}_2^x & -\mathrm{i}\hat{\sigma}_2^y & \hat{\sigma}_2^z & \cdots & \hat{\sigma}_L^x & -\mathrm{i}\hat{\sigma}_L^y & \hat{\sigma}_L^z\end{array}\right) \\ & \cdot \begin{pmatrix} 0 & h & 0 & 0 & 0 & 0 & \cdots & 0 & 0 & 0 \\ h & 0 & -1 & 0 & 0 & 0 & \cdots & 0 & 0 & 0 \\ 0 & -1 & 0 & 0 & 0 & J & \cdots & 0 & 0 & J \\ 0 & 0 & 0 & 0 & h & 0 & \cdots & 0 & 0 & 0 \\ 0 & 0 & 0 & h & 0 & -1 & \cdots & 0 & 0 & 0 \\ 0 & 0 & J & 0 & -1 & 0 & \cdots & 0 & 0 & 0 \\ \vdots & \vdots & \vdots & \vdots & \vdots & \vdots & \ddots & \vdots & \vdots & \vdots \\ 0 & 0 & 0 & 0 & 0 & 0 & \cdots & 0 & h & 0 \\ 0 & 0 & 0 & 0 & 0 & 0 & \cdots & h & 0 & -1 \\ 0 & 0 & J & 0 & 0 & 0 & \cdots & 0 & -1 & 0 \end{pmatrix} \\ & \cdot \left(\begin{array}{cccccccccc}\hat{\sigma}_1^x & \mathrm{i}\hat{\sigma}_1^y & \hat{\sigma}_1^z & \hat{\sigma}_2^x & \mathrm{i}\hat{\sigma}_2^y & \hat{\sigma}_2^z & \cdots & \hat{\sigma}_L^x & \mathrm{i}\hat{\sigma}_L^y & \hat{\sigma}_L^z\end{array}\right)^{\mathrm{T}},\end{aligned} \tag{5}$$

where the superscript T denotes the transpose of the operator vector. The matrix in Eq. (5) can be diagonalized to obtain eigenvalues and corresponding eigenfunctions $\{\lambda_n, u_n\}$ ($n = 1, 2, \ldots, 3L$). With these $\{\lambda_n, u_n\}$ at hand, $\hat{H}$ is reformulated as

$$\hat{H} = \sum_{n=1}^{3L} \hat{H}_n = \sum_{n=1}^{3L} \lambda_n \hat{A}_n^\dagger \hat{A}_n, \tag{6}$$

where the newly obtained operator $\hat{A}_n$ reads

$$\hat{A}_n = \sum_{j=1}^{L} \left[u_{n,3j-2}\hat{\sigma}_j^x + u_{n,3j-1}(\mathrm{i}\hat{\sigma}_j^y) + u_{n,3j}\hat{\sigma}_j^z\right]. \tag{7}$$

It can be observed that $\hat{A}_n$ is a single-body operator encompassing spins from all lattice sites, thus reflecting global information of the system rather than local characteristics. Equation (6) represents the newly formulated Hamiltonian, which is

mathematically fully equivalent to the original one in Eq. (1). All subsequent computations will be based on this new Hamiltonian formulation. Before proceeding to physical observable calculations, we first examine the properties of the obtained Hamiltonian by analyzing the behaviors manifested in $\{\lambda_n, u_n\}$.

### 2.2. The pattern picture

We begin by analyzing the evolution of $\lambda_n$ with respect to $J$ under different longitudinal fields, as illustrated in Fig. 1. For simplicity, we consider a spin chain of length $L = 8$ as a representative example. At $J = 0$, the eigenvalues $\lambda_n$ exhibit three distinct values: one positive, one negative, and one zero. As $J$ increases, the degeneracy is partially lifted, and all lines evolve without any crossings. This allows us to classify $\lambda_n$ into three groups: $\lambda_1$–$\lambda_8$ (lower part), $\lambda_9$–$\lambda_{15}$ (middle part), and $\lambda_{16}$–$\lambda_{24}$ (upper part). Within each group, only the minimum and maximum $\lambda_n$ values remain non-degenerate, while all intermediate states maintain two-fold degeneracy, for instance, in the lower group, the eigenvalues appear as $\lambda_1$, $\lambda_{2,3}$, $\lambda_{4,5}$, $\lambda_{6,7}$ and $\lambda_8$. These features are independent of the longitudinal field strength, as shown in Figs. 1(a)–1(d). Since $\hat{A}_n^\dagger \hat{A}_n$ represents a physical quantity analogous to the occupation number, its projection onto wavefunctions must yield positive values, making $\lambda_n$ qualitatively indicative of the energy hierarchy among different Hamiltonian components $\hat{H}_n$.

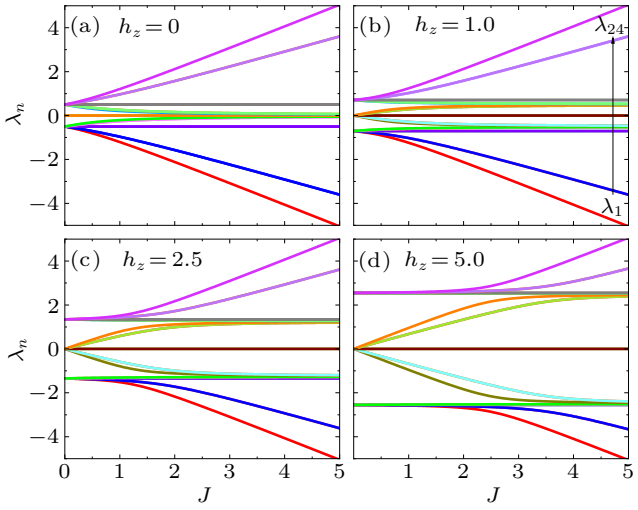



**Fig. 1.** The eigenvalues $\lambda_n$ of the patterns as functions of the Ising interacting strength $J$ for $L = 8$ under different longitudinal fields $h_z = 0$, 1.0, 2.5 and 5.0. The legend in (a)–(d), from bottom to top, corresponds to pattern $\lambda_1$, $\lambda_{2,3}$, $\lambda_{4,5}$, $\lambda_{6,7}$, $\lambda_8$, $\lambda_9$, $\lambda_{10,11}$, $\lambda_{12,13}$, $\lambda_{14,15}$, $\lambda_{16}$, $\lambda_{17}$, $\lambda_{18,19}$, $\lambda_{20,21}$, $\lambda_{22,23}$, $\lambda_{24}$. The patterns are divided into three groups: $\lambda_1$–$\lambda_8$ (lower part), $\lambda_9$–$\lambda_{15}$ (middle part), and $\lambda_{16}$–$\lambda_{24}$ (upper part), which are the same as those grouped by colored-dashed frames in Fig. 2.

Subsequently, we extract the signs (i.e., plus or minus) of the coefficients $u_n = (u_{n,3j-2}, u_{n,3j-1}, u_{n,3j})$ of the spin operators $\{\sigma_j^x, \mathrm{i}\sigma_j^y, \sigma_j^z\}$ in the $\hat{A}_n$ operator, where $\sigma_j^z$ represents the spin state (spin-up/down) and $\sigma_j^x$ and $\mathrm{i}\sigma_j^y$ represent the flip of spins (or dynamical information). These signs are independent of the specific values of the longitudinal field $h_z$ and characterize the relationship between lattice spins; therefore, we call them patterns marked by their corresponding $\lambda_n$, as shown in Fig. 2. All patterns can be divided into three groups, as marked by the dashed red, dashed green and dashed blue frames. These patterns show the following characteristic features.

(i) Except for the patterns $\lambda_{12,13}$ with zero eigenvalue, the patterns with negative eigenvalues have the opposite signs for the coefficients of $\hat{\sigma}_j^x$ and $\mathrm{i}\hat{\sigma}_j^y$, namely, they are out-of-phase; conversely, they are in-phase for the patterns with positive eigenvalues.

(ii) The distinction between different patterns in each group lies in the signs of the coefficients of $\hat{\sigma}_j^z$ and their orders, which correspond to different domains or kinks contained in the patterns.

(iii) For the first group marked by the red frame, the signs of $\hat{\sigma}_i^z$ in the pattern $\lambda_1$ are opposite for nearest neighbor sites, which is a typical characteristic of an antiferromagnetic order with eight-domain; on the contrary, the signs of $\hat{\sigma}_i^z$ in the patterns $\lambda_8$ are the same for all sites, denoting a ferromagnetic order with single-domain. The intermediate patterns have six-, four-, two-domain structures, respectively.

(iv) For the second group, the signs of $\hat{\sigma}_i^z$ are the same as those in the first group, i.e., from the pattern $\lambda_9$ to pattern $\lambda_{16}$, the domain structures are eight-, six-, four-, two-, one-domain. However, their signs of $\hat{\sigma}_j^x$ and $\mathrm{i}\hat{\sigma}_j^y$ are different, which indicates that these two groups of patterns possess the same magnetic order but have different dynamical behaviors.

(v) For the third group, the situation is also the same as that in the first group; however, this group does not play an important role in the ground state due to its higher eigenvalues (seen in Fig. 1), as discussed later.

| | | | | | | | | |
|---|---|---|---|---|---|---|---|---|
| Pattern $\lambda_1$ | (−,+,+) | (+,−,−) | (−,+,+) | (+,−,−) | (−,+,+) | (+,−,−) | (−,+,+) | (+,−,−) |
| Pattern $\lambda_{2,3}$ | (−,+,+) | (−,+,+) | (+,−,−) | (−,+,+) | (+,−,−) | (+,−,−) | (−,+,+) | (+,−,−) |
| Pattern $\lambda_{4,5}$ | (−,+,+) | (−,+,+) | (+,−,−) | (+,−,−) | (−,+,+) | (−,+,+) | (+,−,−) | (+,−,−) |
| Pattern $\lambda_{6,7}$ | (−,+,+) | (−,+,+) | (−,+,+) | (−,+,+) | (+,−,−) | (+,−,−) | (+,−,−) | (+,−,−) |
| Pattern $\lambda_8$ | (−,+,+) | (−,+,+) | (−,+,+) | (−,+,+) | (−,+,+) | (−,+,+) | (−,+,+) | (−,+,+) |
| Pattern $\lambda_9$ | (+,−,+) | (−,+,−) | (+,−,+) | (−,+,−) | (+,−,+) | (−,+,−) | (+,−,+) | (−,+,−) |
| Pattern $\lambda_{10,11}$ | (+,−,+) | (+,−,+) | (−,+,−) | (+,−,+) | (−,+,−) | (−,+,−) | (+,−,+) | (−,+,−) |
| Pattern $\lambda_{12,13}$ | (+,0,+) | (+,0,+) | (−,0,−) | (−,0,−) | (+,0,+) | (+,0,+) | (−,0,−) | (−,0,−) |
| Pattern $\lambda_{14,15}$ | (+,+,+) | (+,+,+) | (+,+,+) | (+,+,+) | (−,−,−) | (−,−,−) | (−,−,−) | (−,−,−) |
| Pattern $\lambda_{16}$ | (+,+,+) | (+,+,+) | (+,+,+) | (+,+,+) | (+,+,+) | (+,+,+) | (+,+,+) | (+,+,+) |
| Pattern $\lambda_{17}$ | (−,−,+) | (+,+,−) | (−,−,+) | (+,+,−) | (−,−,+) | (+,+,−) | (−,−,+) | (+,+,−) |
| Pattern $\lambda_{18,19}$ | (−,−,+) | (−,−,+) | (+,+,−) | (−,−,+) | (+,+,−) | (+,+,−) | (−,−,+) | (+,+,−) |
| Pattern $\lambda_{20,21}$ | (−,−,+) | (−,−,+) | (+,+,−) | (+,+,−) | (−,−,+) | (−,−,+) | (+,+,−) | (+,+,−) |
| Pattern $\lambda_{22,23}$ | (−,−,+) | (−,−,+) | (−,−,+) | (−,−,+) | (+,+,−) | (+,+,−) | (+,+,−) | (+,+,−) |
| Pattern $\lambda_{24}$ | (−,−,+) | (−,−,+) | (−,−,+) | (−,−,+) | (−,−,+) | (−,−,+) | (−,−,+) | (−,−,+) |

**Fig. 2.** The patterns and their relative phases marked by the single-body operators in Eq. (7) with $(\pm,\pm,\pm)$ denoting the signs of $(u_{n,3j-2}, u_{n,3j-1}, u_{n,3j})$ for $L = 8$ under PBC. All patterns are divided into three groups marked by dashed red, dashed green, and dashed blue frames, respectively. For each pattern, a phase factor $\mathrm{e}^{\mathrm{i}\pi}$ is free, not affecting the relative signs within and between patterns.

It is necessary to point out that the nature of the patterns remains unchanged when increasing the system size $L$; that

is to say, the pattern $\lambda_1$ and the pattern $\lambda_L$ always exhibit a $L$-domain structure and a single-domain structure, respectively (for details of patterns' information, one can refer to Ref. [37]). This is the reason that the physics of QPTs can be essentially captured even for small lattice sizes. The finite size effect does not change the physics discussed here qualitatively but does affect the phase boundary quantitatively, as discussed later.

### 2.3. Calculation of physical quantities

After presentation of the pattern picture obtained, we solve Eq. (6) by inserting into the complete basis $|\{\sigma_j^z\}\rangle$ $(j=1,2,\ldots,L)$ with $\hat{\sigma}_j^z|\{\sigma_j^z\}\rangle = \pm_j(\uparrow,\downarrow)|\{\sigma_j^z\}\rangle$. Firstly, we obtain the matrix of the single-body operator $\hat{A}_n$, shown as follows:

$$\left[\hat{A}_n\right]_{\{\sigma_j^z\},\{\sigma_j^z\}'} = \langle\{\sigma_j^z\}|\hat{A}_n|\{\sigma_j^z\}'\rangle, \tag{8}$$

then Eq. (6) can be solved by diagonalizing the matrix obtained by

$$\begin{aligned}\langle\{\sigma_j^z\}|\hat{H}|\{\sigma_j^z\}'\rangle &= \langle\{\sigma_j^z\}|\sum_{n=1}^{3L}\lambda_n\hat{A}_n^\dagger\hat{A}_n|\{\sigma_j^z\}'\rangle \\ &= \sum_{n=1}^{3L}\lambda_n\langle\{\sigma_j^z\}|\hat{A}_n^\dagger\hat{A}_n|\{\sigma_j^z\}'\rangle \\ &= \sum_{n=1}^{3L}\lambda_n\sum_{\{\sigma_j^z\}''}\left[\hat{A}_n^\dagger\right]_{\{\sigma_j^z\},\{\sigma_j^z\}''}\left[\hat{A}_n\right]_{\{\sigma_j^z\}'',\{\sigma_j^z\}'}. \end{aligned} \tag{9}$$

It should be noted that the Hamiltonian matrix $\hat{H}$ here is constructed using the single-body operators $\hat{A}_n$ rather than being built directly. This offers greater simplicity in a numerical implementation, but a detailed discussion about this will not be presented here. After obtaining the eigen-wavefunctions $\Psi_i$ $(i=0,1,\ldots,$ corresponding to the ground state, the first excited state, and so on, respectively), we next project the wavefunction onto different patterns in order to calculate the contributions of different patterns to the physical quantities of interest. For example, the energy contributions of different patterns to the ground state are calculated using the formula

$$\langle\hat{H}_n\rangle = \lambda_n\langle\Psi_0|\hat{A}_n^\dagger\hat{A}_n|\Psi_0\rangle, \quad (n=1,2,\ldots,3L), \tag{10}$$

and the pattern occupancy of the ground state is defined as

$$\langle\hat{O}_n\rangle = \langle\Psi_0|\hat{A}_n^\dagger\hat{A}_n|\Psi_0\rangle, \quad (n=1,2,\ldots,3L). \tag{11}$$

## 3. Properties of the ground state

Before analyzing the properties of the ground state in detail, we first present several low-lying energy levels to provide complete information about the low-lying states and their dependences on the longitudinal field applied, as shown in Fig. 3. The system size is taken as $L=8$. For $h_z=0$ it is very clear that there exists a second-order QPT (see, e.g., Ref. [37]) at $J\sim 1.0$. As $J$ increases, the overall structure of energy levels remains unchanged except for two important points: first, the transition point shifts to larger $J$ values, and second, each energy level rises up to certain $J$ before behaving similarly to the $h_z=0$ case. The larger $h_z$ is, the more pronounced these two features become. What happens in the presence of a finite longitudinal field? Intuitively, a finite $h_z$ aligns all spins along the field direction, which is obviously a paramagnetic phase. With increasing $J$, the paramagnetic phase is gradually suppressed, but a complete antiferromagnetic order does not emerge immediately, which needs a larger $J$. Thus, a second QPT should be expected. In the following we study these two QPTs in detail and identify these three phases through their characteristic patterns.

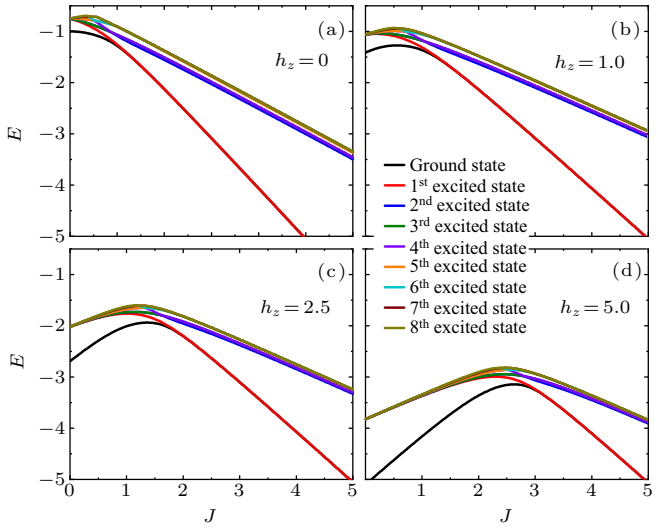



**Fig. 3.** The ground state and the first eight excited states energies of the transverse antiferromagnetic Ising model in the absence (a) and presence (b)–(d) of longitudinal fields. The system size is taken as $L=8$.

### 3.1. Pattern description of the ground state

Figures 4(a1)–4(d1) present the ground state energy $E_0$ (black solid curves) and their components $H_n$ (colored solid curves, calculated by Eq. (10)) as functions of the interaction $J$ with $h_z=0,1.0,2.5$ and 5.0, respectively. The system size is taken as $L=8$. The circles represent the results of numerical exact diagonalization, which confirms the validity of the pattern formulation. In the absence of $h_z$ shown in Figs. 4(a1) and 4(a2), the antiferromagnetic Ising model is essentially equivalent to its ferromagnetic counterpart,[37] which is plotted here for comparison.

Turning to the cases of finite $h_z$, the role played by the longitudinal field is apparent as follows.

(i) The dominant role of the component $H_1$ marked by red curves is obviously delayed with increasing $h_z$.

(ii) The effect of the component $H_8$ marked by green curves is significantly enhanced, which shows a strong response to the longitudinal field, crossing lower-energy com-

ponents $H_{2,3}$, $H_{4,5}$, $H_{6,7}$ and eventually intersecting $H_1$, thus playing a dominant role starting from a certain $h_z$ for a region of $J$ [see, e.g., Figs. 4(c2) and 4(d2)]. This behavior is physically justified since $H_8$ corresponds to the pattern $\lambda_8$ which has a ferromagnetic character (shown in Fig. 2). Therefore, the pattern $\lambda_8$ precisely reflects the characteristic effect of the longitudinal field, as it tends to align all spins in the same direction.

(iii) In addition to $H_8$, $H_{16}$ marked by orange curves also exhibits a strong response to the longitudinal field. Unlike $H_8$, however, $H_{16}$ possesses positive energy. In the small $J$ region, $H_{16}$ increases linearly with $J$, following the same trend as the total energy, indicating that the total energy primarily originates from $H_{16}$'s contribution. This linear increase becomes more pronounced with larger $h$ values, as clearly shown in Figs. 4(c2) and 4(d2). According to Fig. 2, the pattern $\lambda_{16}$ also displays ferromagnetic characteristics. Consequently, under the longitudinal field applied, both pattern $\lambda_8$ and pattern $\lambda_{16}$ become excited: while $H_8$ with its negative energy characterizes the system's phase, $H_{16}$ effectively serves as the background contribution induced by the longitudinal field.

(iv) At large enough $J$ the system eventually enters the antiferromagnetic phase and $H_1$ becomes dominant, as shown in Fig. 4(d1). This transition can be characterized by the second derivative of the total energy, as manifested by the dip at $J_c$ shown in Figs. 4(a3)–4(d3).

(v) Therefore, the phase of the ground state can be determined by combining both the crossing point of $H_1$ and $H_8$ and the second derivative of the total energy. It should be noted that when $J$ exceeds $J_b$, the system does not immediately enter the antiferromagnetic phase; instead, it remains in a disordered phase within the $J_b - J_c$ interval. Only when $J$ surpasses $J_c$ does the system transition into the antiferromagnetic phase.

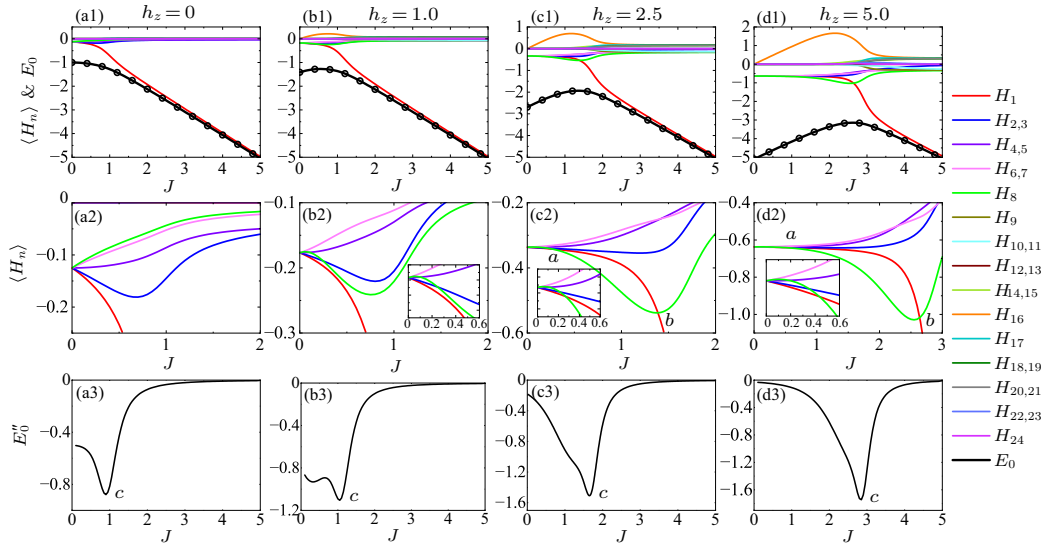



**Fig. 4.** (a1)–(d1) The ground state energies $E_0$ (black curves) and their components $H_n$ (colored curves) as functions of $J$ for $h_z = 0, 1.0, 2.5$ and 5.0. (a2)–(d2) The enlarged views of energy components. Points $a$ and $b$ are the intersections of $H_1$ and $H_8$. (a3)–(d3) The second derivatives of the total energy. A dip at point $c$ indicates the position at which there occurs a QPT. $L = 8$ is taken.

### 3.2. Large system sizes

We now extend the above analysis to larger system sizes from $L = 16$ to 128. Figure 5 shows the enlarged views of energy components under different longitudinal fields, where the red curves represent $H_1$ (whose pattern exhibits antiferromagnetic order character) and the green curves represent $H_L$ ($L = 16, 32, 64, 128$, with patterns showing ferromagnetic order character). The following can be found.

(i) As the longitudinal field increases, $H_L$ decreases continuously. Beyond a critical field strength, its energy becomes lower than $H_1$, dominating the ground state configuration.

(ii) The behavior of $H_L$ is size-dependent: at $h_z = 0.5$, while $H_1$ and $H_L$ show no crossing for $L = 16$, they exhibit clear intersections for $L = 32, 64$, and 128.

(iii) The significance of $H_L$ becomes particularly pronounced for large system sizes and strong fields, as evidenced in Fig. 5(d5). The inset shows the second derivative of total energy. The crossing point between $H_1$ and $H_L$ does not precisely coincide with the dip position, indicating that there exists an intermediate phase, namely, the disordered phase.

(iv) These results lead to two distinct phase transition pathways. For weak fields (small $h_z$) where $H_1$ and $H_L$ do not cross, the system transitions directly from the disordered phase to the antiferromagnetic phase. For stronger fields (large $h_z$) where $H_L$ dominates $H_1$, the system progresses sequentially through paramagnetic $\rightarrow$ disordered $\rightarrow$ antiferromagnetic phase transitions.

We have also calculated another physical quantity, the pattern occupation, using Eq. (11), as shown in Fig. 6, where we set the system size to $L = 128$. Although the number of patterns is $3L$, only three patterns are significant: the pattern $\lambda_1$ (red curves, with antiferromagnetic order character), the pattern $\lambda_L$ (green curves, with ferromagnetic order character), and the pattern $\lambda_{2L}$ (orange curves, with ferromagnetic

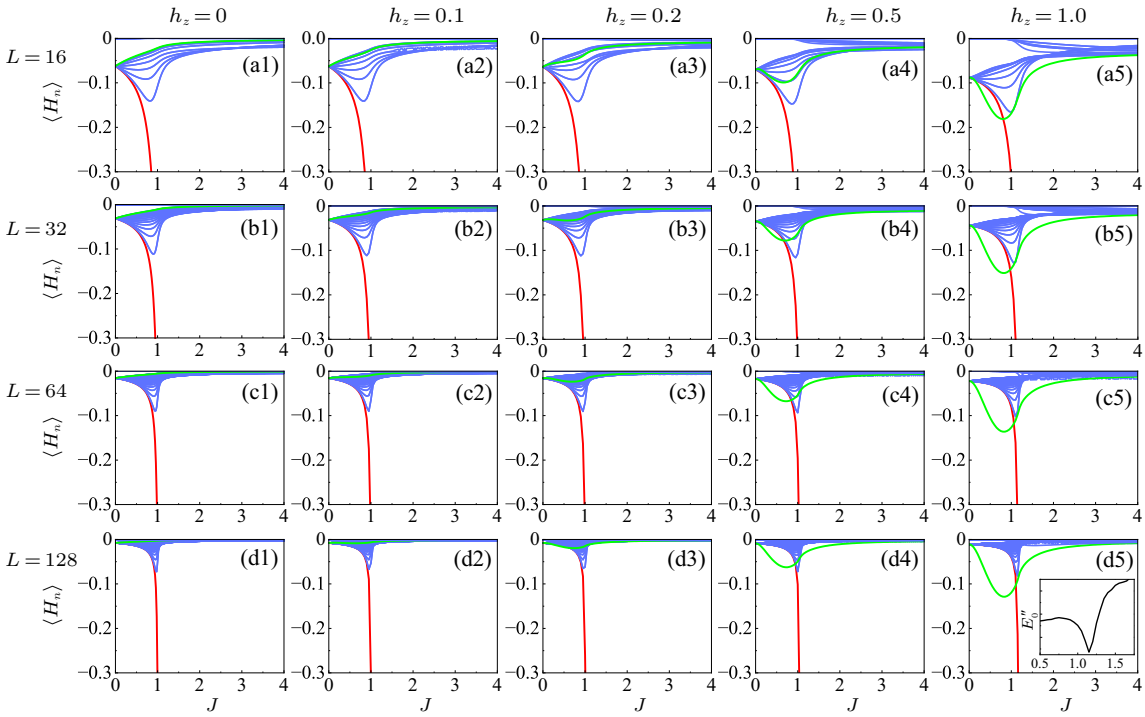



**Fig. 5.** The enlarged views of energy components $H_n$ for large sizes from $L = 16$ to 128 with $h_z = 0, 0.1, 0.2, 0.5$ and 1.0. The different longitudinal fields are taken in order to show more clearly the evolution of the $H_L$ component (green curves) and the red ones are for $H_1$. The inset in (d5) is the second derivative of the total energy.

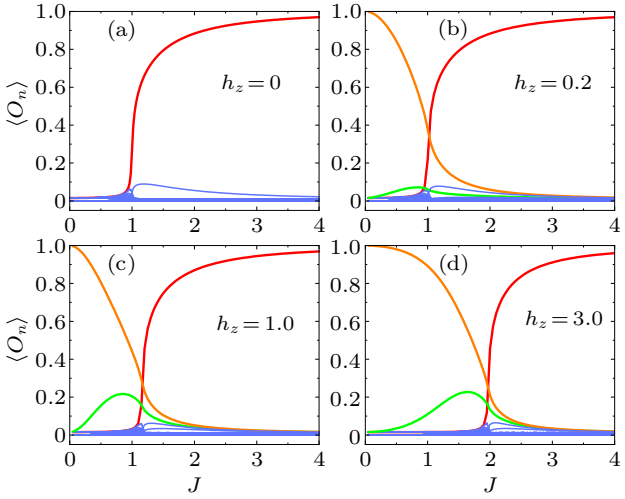



**Fig. 6.** The pattern occupancy of the ground state for different longitudinal fields $h_z = 0, 0.2, 1.0$, and 3.0 for system size $L = 128$. Red, green and orange curves represent the pattern $\lambda_1$, the pattern $\lambda_L$ and the pattern $\lambda_{2L}$, respectively.

order character), while the contributions from other patterns approach essentially to zero with increasing lattice size. At $h_z = 0$, the model reduces to the transverse-field Ising model, where only pattern $\lambda_1$ plays a significant role, increasing with $J$. For finite $h_z$, the behavior of the pattern $\lambda_1$ remains largely unchanged, merely shifting rightward as $h_z$ increases, whereas both the pattern $\lambda_L$ and pattern $\lambda_{2L}$ exhibit positive responses to the longitudinal field: the pattern $\lambda_L$ gradually increases from zero, while the pattern $\lambda_{2L}$ decreases from one. Thus, the pattern picture visually demonstrates the effect of the longitudinal field on the system, namely, the excitation of the pattern $\lambda_L$ and pattern $\lambda_{2L}$ with ferromagnetic character, which may be observed on suitable quantum simulation platforms. Additionally, it should be noted that the pattern $\lambda_L$ has negative energy [$H_L$, see green curves in Figs. 5(d1)–5(d5)], determining the phases of the ground state, while the pattern $\lambda_{2L}$ has positive energy (not shown here) and represents the background contribution from the longitudinal field. This is consistent with the previous analysis for $L = 8$.

Based on the above analysis, it is evident that the antiferromagnetic Ising model exhibits significantly richer behavior compared to its ferromagnetic counterpart. In the ferromagnetic case, the introduction of a longitudinal field suppresses ground state phase transitions.[37] On the contrary, in the antiferromagnetic system, the longitudinal field cannot eliminate phase transitions, instead, it exhibits three phases: the paramagnetic phase, the disordered phase and the antiferromagnetic phase. This is because the effect of the uniform longitudinal field is somehow frustrated by the antiferromagnetic interaction. Thus in a really frustrated system, e.g., the axial next-nearest-neighbor Ising model, a richer behavior will be observed.[38]

## 4. Conclusion

We employ the pattern picture to investigate QPTs in the transverse antiferromagnetic Ising model under a longitudinal field. The patterns are obtained by diagonalizing the model's Hamiltonian in operator space. Among these, the pattern $\lambda_1$ representing AFM order and the pattern $\lambda_L$ representing FM order play key roles in characterizing the phases of the system. Our results reveal the existence of three distinct phases: the antiferromagnetic phase, the disordered phase, and the paramagnetic phase. For a small $h_z$, the system transitions from the

disordered phase to the AFM phase as $J$ increases. For a large $h_z$, the system undergoes sequentially through paramagnetic $\rightarrow$ disordered $\rightarrow$ antiferromagnetic phases. These findings affirm the validity of our method. Results for larger lattice sizes and the full phase diagram will be presented in the future.

It is also noteworthy that the disordered phase had long been overlooked until a recent study identified its existence using the quantum fidelity method.[30] Our approach provides independent confirmation of the disordered phase in this model. Moreover, the existence of this phase should be confirmed by available quantum simulations such as spin chains in optical lattices,[11] trapped ions,[12,16] and Rydberg atom systems,[39,40] and so on.

## Acknowledgements

The work is partly supported by the National Key Research and Development Program of China (Grant No. 2022YFA1402704) and the National Natural Science Foundation of China (Grant No. 12247101).

## References

[1] Lenz W 1920 *Physikalische Zeitschrift* **21** 613
[2] Ising E 1925 *Zeitschrift für Physik* **31** 253
[3] Niss M 2005 *Archive for History of Exact Sciences* **59** 267
[4] Stanley H E 1987 *Introduction to Phase Transitions and Critical Phenomena* (Oxford: Oxford University Press)
[5] Kondepudi D and Prigogine I 1998 *Modern Thermodynamics–From Heat Engines to Dissipative Systems* (Chichester: Wiley)
[6] Chaikin P M and Lubensky T C 2000 *Principles of Condensed Matter Physics* (Cambridge University Press)
[7] Sachdev S 2011 *Quantum phase transitions* 2nd Edn. (Cambridge: Cambridge University Press)
[8] Suzuki S, ichi Inoue J and Chakrabarti B K 2013 *Quantum Ising Phases and Transitions in Transverse Ising Models* (ADS)
[9] Dutta A, Aeppli G, Chakrabarti B K, Divakaran U, Rosenbaum T F and Sen D 2015 *Quantum Phase Transitions in Transverse Field Spin Models: From Statistical Physics to Quantum Information* (Cambridge University Press)
[10] Friedenauer A, Schmitz H, Glueckert J T, Porras D and Schaetz T 2008 *Nat. Phys.* **4** 757
[11] Simon J, Bakr W S, Ma R, Tai M E, Preiss P M and Greiner M 2011 *Nature* **472** 307
[12] Islam R, Edwards E, Kim K, Korenblit S, Noh C, Carmichael H, Lin G D, Duan L M, Joseph Wang C C, Freericks J and Monroe C 2011 *Nat. Commun.* **2** 377
[13] Kim K, Korenblit S, Islam R, Edwards E E, Chang M S, Noh C, Carmichael H, Lin G D, Duan L M, Wang C C J, Freericks J K and Monroe C 2011 *New J. Phys.* **13** 105003
[14] Lewenstein M, Sanpera A and Ahufinger V 2012 *Ultracold Atoms in Optical Lattices: Simulating Quantum Many-body Systems* (Oxford: Oxford University Press)
[15] Georgescu I M, Ashhab S and Nori F 2014 *Rev. Mod. Phys.* **86** 153
[16] Monroe C, Campbell W C, Duan L M, Gong Z X, Gorshkov A V, Hess P W, Islam R, Kim K, Linke N M, Pagano G, Richerme P, Senko C and Yao N Y 2021 *Rev. Mod. Phys.* **93** 025001
[17] Scholl P, Schuler M, Williams H J, Eberharter A A, Barredo D, Schymik K N, Lienhard V, Henry L P, Lang T C, Lahaye T, Laeuchli A M and Browaeys A 2021 *Nature* **595** 233
[18] Kadowaki T and Nishimori H 1998 *Phys. Rev. E* **58** 5355
[19] Das A and Chakrabarti B K 2008 *Rev. Mod. Phys.* **80** 1061
[20] Johnson M W, Amin M H S, Gildert S, Lanting T, Hamze F, Dickson N, Harris R, Berkley A J, Johansson J, Bunyk P, Chapple E M, Enderud C, Hilton J P, Karimi K, Ladizinsky E, Ladizinsky N, Oh T, Perminov I, Rich C, Thom M C, Tolkacheva E, Truncik C J S, Uchaikin S, Wang J, Wilson B and Rose G 2011 *Nature* **473** 194
[21] Graß T 2019 *Phys. Rev. Lett.* **123** 120501
[22] Onsager L 1944 *Phys. Rev.* **65** 117
[23] Wilson K G 1975 *Rev. Mod. Phys.* **47** 773
[24] Pfeuty P 1970 *Annals of Physics* **57** 79
[25] Sen P 2000 *Phys. Rev. E* **63** 016112
[26] Ovchinnikov A A, Dmitriev D V, Krivnov V Y and Cheranovskii V O 2003 *Phys. Rev. B* **68** 214406
[27] Lajkó P, d'Auriac J C A, Rieger H and Iglói F 2020 *Phys. Rev. B* **101** 024203
[28] Lajkó P and Iglói F 2021 *Phys. Rev. B* **103** 174404
[29] Lin Y P, Kao Y J, Chen P and Lin Y C 2017 *Phys. Rev. B* **96** 064427
[30] Bonfim O F d A, Boechat B and Florencio J 2019 *Phys. Rev. E* **99** 012122
[31] Thouless D J 1969 *Phys. Rev.* **187** 732
[32] Anderson P W and Yuval G 1969 *Phys. Rev. Lett.* **23** 89
[33] Bar A and Mukamel D 2014 *Phys. Rev. Lett.* **112** 015701
[34] Sheinman M, Sharma A, Alvarado J, Koenderink G H and MacKintosh F C 2015 *Phys. Rev. Lett.* **114** 098104
[35] Alert R, Tierno P and Casademunt J 2017 *Proc. Natl. Acad. Sci. USA* **114** 12906
[36] Gross B, Bonamassa I and Havlin S 2022 *Phys. Rev. Lett.* **129** 268301
[37] Yang Y T, Chen F Z and Luo H G 2025 *Phys. Rev. E* **112** 044102
[38] Yang Y T, Chen F Z and Luo H G arXiv: 2301.08891
[39] Bernien H, Schwartz S, Keesling A, Levine H, Omran A, Pichler H, Choi S, Zibrov A S, Endres M, Greiner M, Vuletic V and Lukin M D 2017 *Nature* **551** 579
[40] Keesling A, Omran A, Levine H, Bernien H, Pichler H, Choi S, Samajdar R, Schwartz S, Silvi P, Sachdev S, Zoller P, Endres M, Greiner M, Vuletić V and Lukin M D 2019 *Nature* **568** 207